NANO LETTERS

pubs.acs.org/NanoLett Letter

Reversible Transition of Semiconducting $PtSe_2$ and Metallic $PtTe_2$ for Scalable All-2D Edge-Contacted FETs

Sang Sub Han, Shahid Sattar, Dmitry Kireev, June-Chul Shin, Tae-Sung Bae, Hyeon Ih Ryu, Justin Cao, Alex Ka Shum, Jung Han Kim, Carlo Maria Canali, Deji Akinwande, Gwan-Hyoung Lee, Hee-Suk Chung,* and Yeonwoong Jung*

Cite This: *Nano Lett.* 2024, 24, 1891−1900 Read Online

ACCESS | Metrics & More | Article Recommendations | Supporting Information

ABSTRACT: Two-dimensional (2D) transition metal dichalcogenide (TMD) layers are highly promising as field-effect transistor (FET) channels in the atomic-scale limit. However, accomplishing this superiority in scaled-up FETs remains challenging due to their van der Waals (vdW) bonding nature with respect to conventional metal electrodes. Herein, we report a scalable approach to fabricate centimeter-scale all-2D FET arrays of platinum diselenide ($PtSe_2$) with in-plane platinum ditelluride ($PtTe_2$) edge contacts, mitigating the aforementioned challenges. We realized a reversible transition between semiconducting $PtSe_2$ and metallic $PtTe_2$ via a low-temperature anion exchange reaction compatible with the back-end-of-line (BEOL) processes. All-2D $PtSe_2$ FETs seamlessly edge-contacted with transited metallic $PtTe_2$ exhibited significant performance improvements compared to those with surface-contacted gold electrodes, e.g., an increase of carrier mobility and on/off ratio by over an order of magnitude, achieving a maximum hole mobility of ~50.30 $cm^2\ V^{-1}\ s^{-1}$ at room temperature. This study opens up new opportunities toward atomically thin 2D-TMD-based circuitries with extraordinary functionalities.

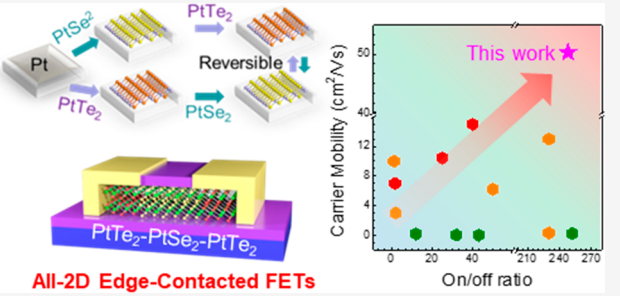

KEYWORDS: *2D $PtTe_2$ layer, 2D $PtSe_2$ layer, anion exchange, chemical transition, edge contact, 2D TMD heterostructure*

2D semiconducting TMD layers have garnered significant attention as promising FET channels in the scaling-down trend of semiconductor industry owing to their high carrier mobilities and exceptional gating characteristics.[1−4] However, performances of 2D TMD FETs have been significantly limited by high interfacial resistances between 2D channels and deposited metal electrodes, e.g., uncontrollable Schottky barrier,[4−6] Fermi level pinning,[7−10] and large contact resistance.[3,4,11] To address these challenges, substantial efforts have been driven by exploring chemical doping and physical contact engineering.[3,11−16] Among them, the "2D−2D edge contact" approach to construct the in-plane heterolayers between 2D semiconducting channels and 2D metallic electrodes is considered promising as it can eliminate the channel/electrode vdW gaps which act as tunnel barriers.[3,11−16] Recently, chemical vapor deposition (CVD) approaches have been explored to create such 2D−2D edge contacts, employing the chemical conversion between 2D channel and electrode materials.[17−21] However, they often require the complicated processes combining the mechanical exfoliation of 2D layers and their subsequent treatments.[18] This complexity limits scalability in device fabrication and compatibility with complementary metal-oxide semiconductor (CMOS) processes.

Herein, we developed a facile, viable, and scalable strategy to fabricate FET arrays constituting semiconducting 2D channels edge-contacted with metallic 2D electrodes. We employed wafer-scale CVD-grown semiconducting 2D $PtSe_2$ layers as FET channels and demonstrated their reversible chemical/electrical transition to metallic 2D $PtTe_2$ layers via the controlled Se−Te exchange reaction. All processes associated with the growth and transformation of 2D materials were conducted at low temperatures, compatible with the BEOL/CMOSS processes. 2D $PtSe_2$ FETs edge-contacted with 2D $PtTe_2$ metallic electrodes exhibited greatly improved performances compared with their counterparts with surface contacts of gold (Au).

Figure 1a illustrates a schematic of a single array of all-2D vdW heterolayers, in which semiconducting 2D $PtSe_2$ channels are seamlessly interfaced with metallic 2D $PtTe_2$ electrodes. Figure 1b depicts the procedures to grow wafer-scale 2D $PtSe_2$

Received: September 23, 2023
Revised: December 21, 2023
Accepted: December 22, 2023
Published: December 27, 2023

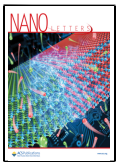

https://doi.org/10.1021/acs.nanolett.3c03666
Nano Lett. 2024, 24, 1891−1900

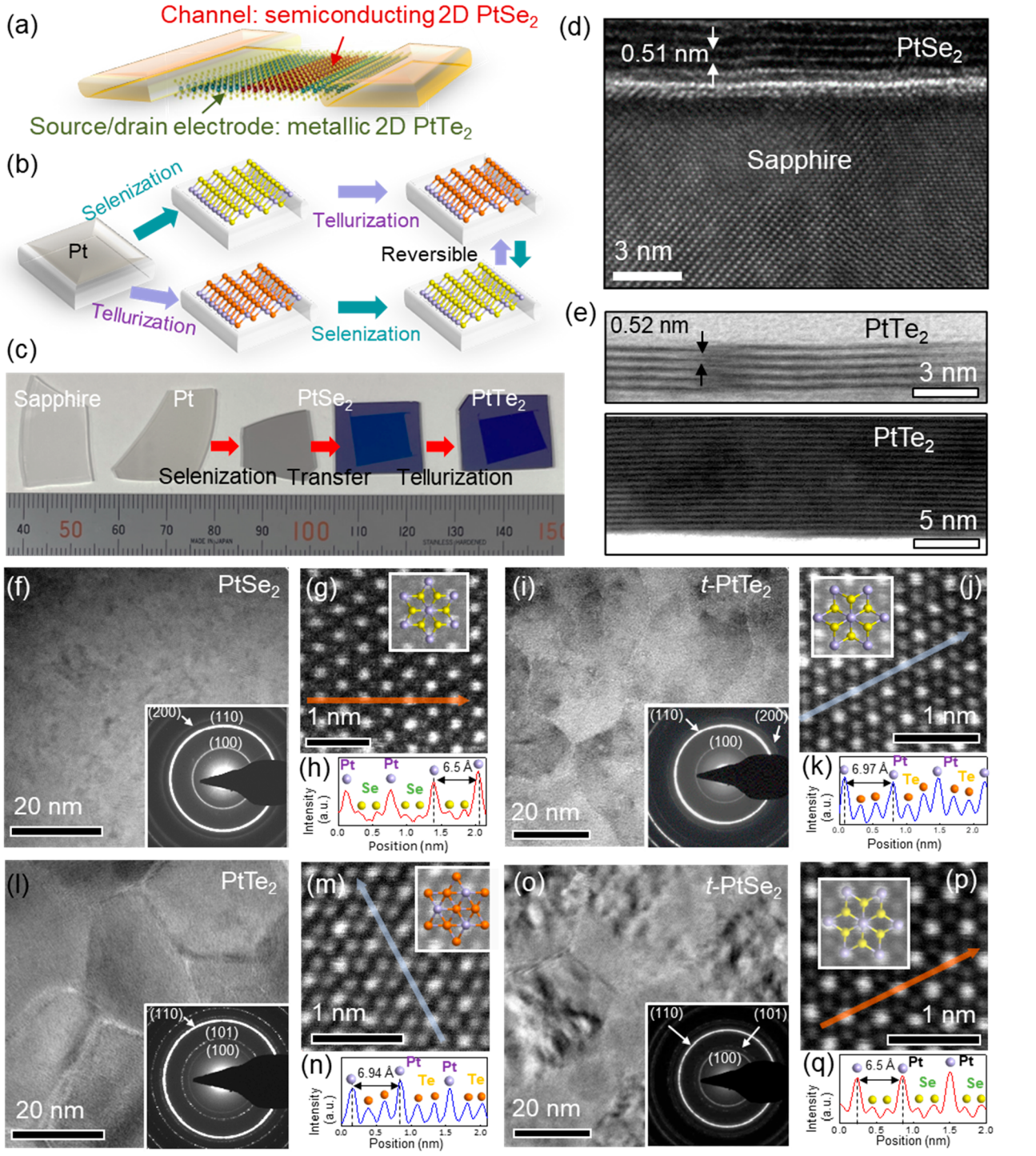

Figure 1. (a) Schematic illustration of all-2D vdW heterolayers with in-plane edge contacts containing semiconducting 2D $PtSe_2$ layers seamlessly interfaced with 2D $PtTe_2$ layers. (b) Schematic illustration of the chemical reaction process for the reversible trasition of 2D $PtSe_2$ layers and 2D $PtTe_2$ layers. (c) Camera image of samples prepared at each sample preparation stage. (d, e) Cross-sectional HR-TEM images of (d) 2D $PtSe_2$ layers on a sapphire wafer and (e) layer-number-controlled 2D $PtTe_2$ layers on a SiO_2/Si wafer. (f–k) Structural analysis for the transition of 2D $PtSe_2$ layers to 2D $PtTe_2$ layers. (f) Low-magnification plane-view TEM image and corresponding SAED pattern (inset), (g) plane-view HR-STEM image, and (h) digital micrograph intensity profile corresponding to the line in (g), obtained from pristine 2D $PtSe_2$ layers before their transition. (i) Low-magnification plane-view TEM image and corresponding SAED pattern (inset), (j) plane-view HR-STEM image, and (k) digital micrograph intensity profile corresponding to the line in (j), obtained from 2D $PtTe_2$ layers after their transition from 2D $PtSe_2$ layers. (l–q) Structural analysis for the transition of 2D $PtTe_2$ layers to 2D $PtSe_2$ layers. (l) Low-magnification plane-view TEM image and corresponding SAED pattern (inset), (m) plane-view HR-STEM image, and (n) digital micrograph intensity profile corresponding to the line in (l), obtained from pristine 2D $PtTe_2$ layers before their transition. (o) Low-magnification plane-view TEM image and corresponding SAED pattern (inset), (p) plane-view HR-STEM image, and (q) digital micrograph intensity profile correspomdig to the line in (j), obtained from 2D $PtSe_2$ layers after their transition from 2D $PtTe_2$ layers.

https://doi.org/10.1021/acs.nanolett.3c03666
Nano Lett. 2024, 24, 1891−1900

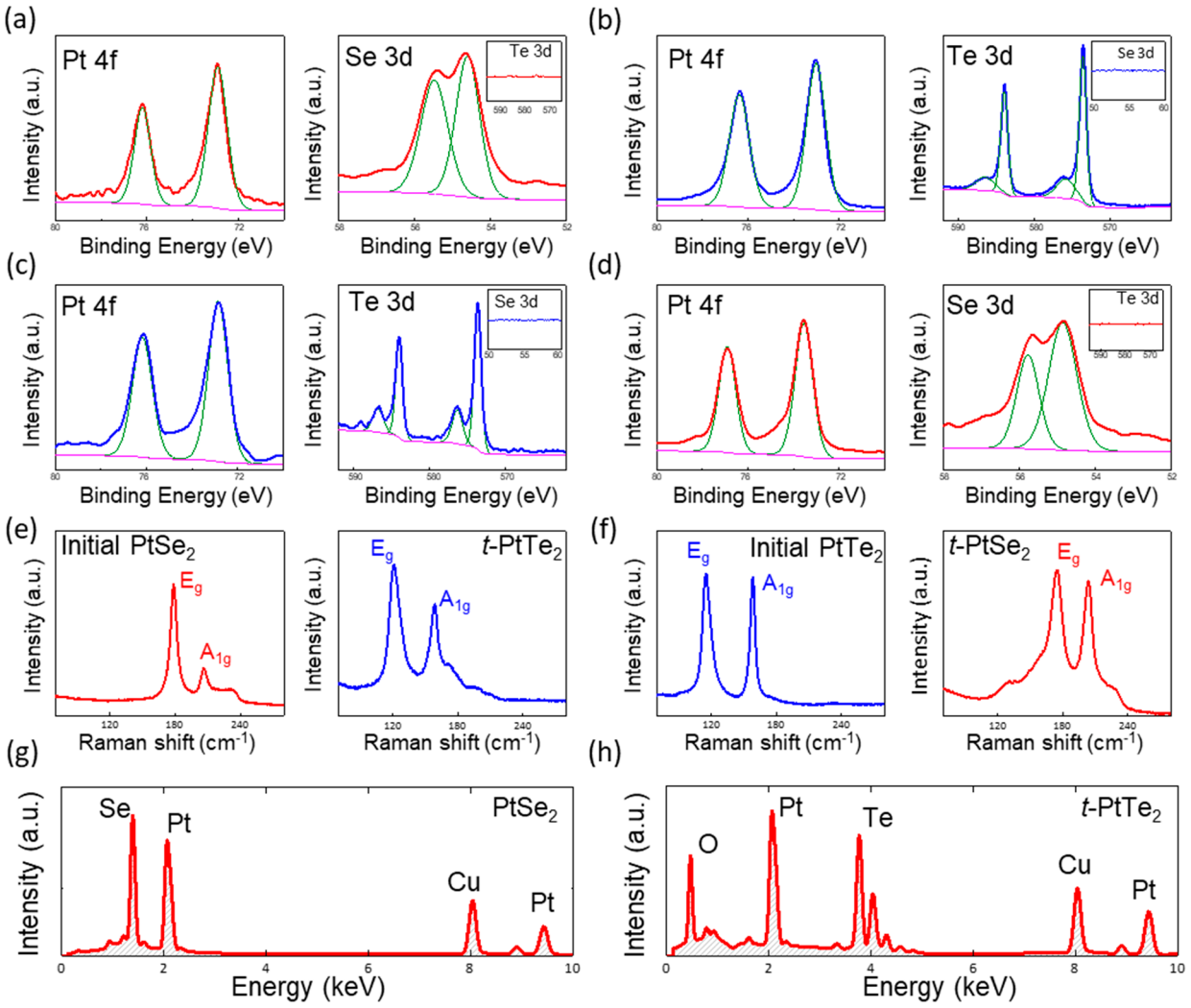

Figure 2. (a, b) XPS spectra showing Pt 4f, Se 3d, and Te 3d obtained from 2D $PtSe_2$ layers (a) before and (b) after their transition to 2D $PtTe_2$ layers. (c, d) XPS spectra showing Pt 4f, Se 3d, and Te 3d obtained from 2D $PtTe_2$ layers (c) before and (d) after their transition to 2D $PtSe_2$ layers. (e, f) Raman profiles of (e) 2D $PtSe_2$ layers before (left) and after (right) their transition and (f) 2D $PtTe_2$ layers before (left) and after (right) their transition. (g, h) EDS spectra obtained from (g) 2D $PtSe_2$ layers and (h) 2D *t*-$PtTe_2$ layers.

layers and 2D $PtTe_2$ layers and their reversible transitions via CVD reactions. Details on the CVD growth/reactions are described in the Supporting Information, Experimental Section. Briefly, Pt-film-deposited substrates undergo thermal selenization or tellurization for the growth of 2D $PtSe_2$ or 2D $PtTe_2$ layers at 350−400 °C, using vaporized selenium or tellurium precursors, respectively. For the transition reaction, as-grown 2D $PtSe_2$ or 2D $PtTe_2$ layers are subsequently tellurized or selenized, respectively, via the same CVD conditions adopted for their growth. Figure 1c shows a camera image demonstrating the entire sample preparation procedure adopted for the $PtSe_2$-to-$PtTe_2$ transition, including CVD reactions and layer transfers (Supporting Information, Experimental Section). With as-grown 2D layers before their transition, we first confirmed their morphology-controlled growth on diverse substrates. Figure 1d shows a cross-sectional high-resolution transmission electron microscope (HR-TEM) image of 2D $PtSe_2$ layers grown on a sapphire wafer, revealing well-resolved vdW gaps of 0.51 nm and a layer number of ∼5. Figure 1e shows cross-sectional HR-scanning TEM (STEM) images of two different samples of 2D $PtTe_2$ layers grown on SiO_2/Si wafers taken in bright-field (top) and dark-field (bottom) imaging modes. Two distinct 2D layer numbers of ∼5 (top) and ∼25 (bottom) are observed, which was achieved by controlling the thickness of Pt films as reported in our previous studies, i.e., Pt thickness of ∼1.2 and ∼5 nm, respectively.[22−27] Following the layer-controlled growth, we performed atomic-scale structural characterizations of materials before/after their reversible transition. Figure 1f−k presents the TEM analysis for the samples corresponding to the transition of $PtSe_2$ to $PtTe_2$. Figure 1f shows a low-magnification plane-view TEM image of as-grown 2D $PtSe_2$ layers, confirming their large-area continuous growth. The inset shows the corresponding selected area electron diffraction (SAED) pattern revealing the dominance of (100), (110), and (200) planes, which indicates the horizontal orientation of their basal planes as previously reported.[22,28] Figure 1g shows a plane-view HR-STEM image of 2D $PtSe_2$ layers along with an overlaid atomic structure model visualizing an octahedral configuration of one centered Pt atom surrounded by six Se atoms corresponding to the CdI_2-type structure (trigonal; $P\bar{3}m1$ space group) 2D layers.[22,23,29] Figure 1h presents the intensity profile corresponding to the orange line in Figure 1g, indicating a periodic repetition of two Se atoms between a Pt

https://doi.org/10.1021/acs.nanolett.3c03666
Nano Lett. 2024, 24, 1891−1900

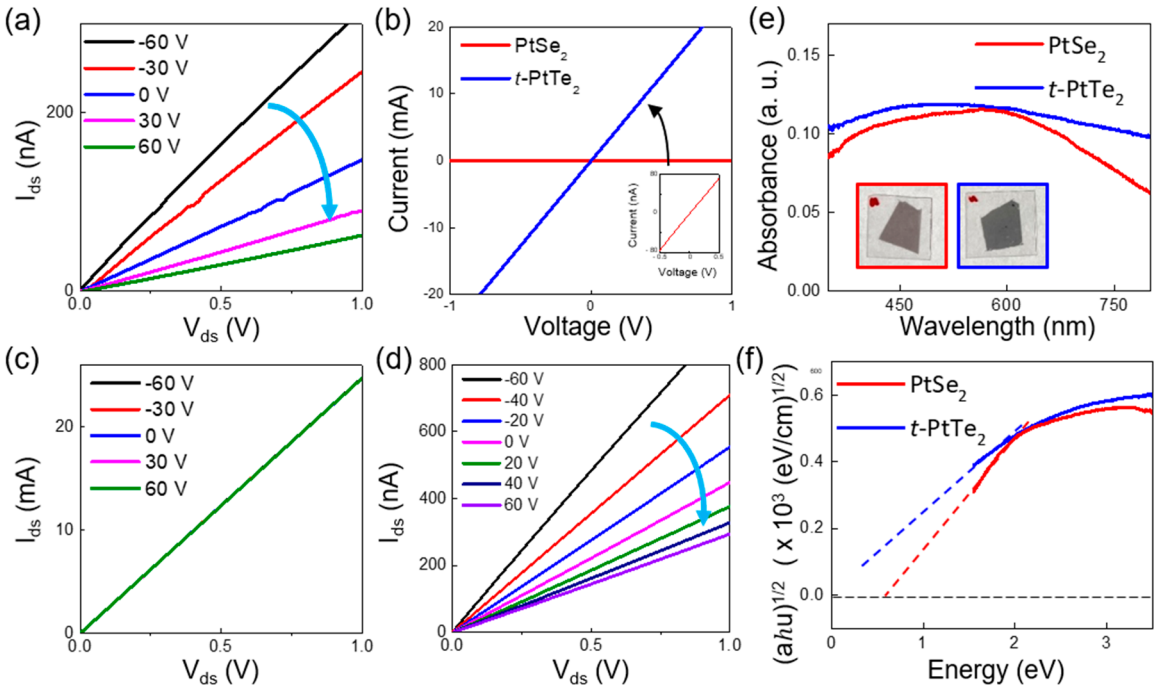

Figure 3. (a) FET I_{ds}−V_{ds} transfer curve of pristine 2D $PtSe_2$ layers, indicating a p-type semiconducting transport. (b) I−V characteristics of 2D $PtSe_2$ layers before (red) and after (blue) their transition to 2D t-$PtTe_2$ layers along with a magnified view of the I−V curve before the transition (inset). (c) FET I_{ds}−V_{ds} transfer curve obtained of 2D t-$PtTe_2$ layers, indicating a metallic transport. (d) FET I_{ds}−V_{ds} transfer curve of 2D t-$PtSe_2$ layers transited from 2D $PtTe_2$ layers. (e) Optical absorbance spectra of 2D $PtSe_2$ layers on willow glasses before (red) and after (blue) their transition to 2D t-$PtTe_2$ layers along with the corresponding sample images (inset). (f) Tauc plots extracted from the optical absorbance spectra in (e).

atom. The measured distance between each Pt atom is 6.5 Å, which well agrees with previous studies.[22,23,29] Figure 1i shows a low-magnification plane-view TEM image of 2D $PtTe_2$ layers transited from 2D $PtSe_2$ layers along with the indexed SAED pattern (inset), a combination of which confirms the horizontal alignment of the transited-$PtTe_2$ (i.e., t-$PtTe_2$) layers. Figure 1j displays a plane-view HR-STEM image of the 2D t-$PtTe_2$ layers along with the corresponding atomic structure, revealing their octahedral structure is identical to that of 2D $PtSe_2$ layers before transition. Figure 1k presents the intensity profile corresponding to the blue line in Figure 1j indicating the periodic arrangement of Se and Pt atoms, consistent with previous studies.[27,30,31] These comprehensive characterizations confirm that the structural integrity of the 2D layers corresponding to the $PtSe_2$-to-$PtTe_2$ transition is well preserved during the Se-to-Te anion exchange reaction. Furthermore, we identified the average grain sizes of 2D $PtSe_2$ and 2D t-$PtTe_2$ layers with their plane-view STEM images (Supporting Information, Figure S1). We then performed TEM characterizations of the materials which underwent the chemical reaction in the opposite direction, i.e., the $PtTe_2$-to-$PtSe_2$ transition (Figure 1l−n). Specifically, parts l, m, and n of Figure 1 present plane-view TEM/SAED, HR-STEM, and intensity profiles of 2D $PtTe_2$ layers before their transition to 2D $PtSe_2$ layers, respectively. The analysis comprehensively confirms the high crystallinity of 2D $PtTe_2$ layers in their pristine state, consistent with previous studies.[27,30,31] Figure 1o−q presents the TEM analysis for the 2D $PtTe_2$ layers after their transition to 2D $PtSe_2$ layers, i.e., plane-view TEM/SAED (Figure 1o), HR-STEM (Figure 1p), and intensity profile (Figure 1q), all of which support the complete transition of 2D $PtTe_2$ layers to 2D $PtSe_2$ layers with preserved crystallinity.[26,27,29,32] This highly reversible structural transition between $PtSe_2$ and $PtTe_2$ layers is attributed to their nearly identical crystalline structure, i.e., lattice parameters of a = 3.8 Å, c = 5.1 Å for $PtSe_2$[33,34] and a = 4.0 Å, c = 5.2 Å for $PtTe_2$[33−35] in the identical CdI_2-type structure, which indicates an insignificant degree of any lattice distortion involving their transition.

Following the TEM microstructural analysis, we performed various macroscale spectroscopic characterizations to verify the transition-associated chemical composition change. Figure 2a−d presents X-ray photoelectron spectroscopy (XPS) analyses for the materials undergoing the transition of $PtSe_2$ to $PtTe_2$ (Figure 2a,b) vs $PtTe_2$ to $PtSe_2$ (Figure 2c,d). Figure 2a presents the binding energies for the Pt 4f (left) and Se 3d (right) orbitals obtained from pristine 2D $PtSe_2$ layers in which the energy values of Pt $4f_{5/2}$, Pt $4f_{7/2}$, Se $3d_{3/2}$, and Se $3d_{5/2}$ at 76.2, 72.9, 55.4, and 54.6 eV, respectively, are consistent with previous observations.[22,23,25] The atomic ratio of Pt:Se calculated from the XPS spectra is ∼33:67, indicating the stoichiometric growth of 2D $PtSe_2$ layers. Figure 2b presents the core-level XPS profiles of Pt and Te obtained from the same 2D $PtSe_2$ layers after their transition to the 2D t-$PtTe_2$ layers. While Figure 2b (left) exhibits the binding energies of Pt $4f_{5/2}$ and Pt $4f_{7/2}$ at 76.4 and 73.0 eV, respectively, the XPS spectrum in Figure 2b (right) exhibits Te 3d binding energy peaks at 583.9 and 573.5 eV corresponding to Te (IV) as well as additional peaks corresponding to Te (0) at 586.5 and 576.2 eV, consistent with previous studies on pristine 2D $PtTe_2$ layers.[24,26,27] Also, it is noteworthy that all of these Te-associated peaks were absent in the XPS spectra of the initial 2D $PtSe_2$ layers before their transition but appeared only after the transition. Furthermore, it is remarkable to note that the Se

https://doi.org/10.1021/acs.nanolett.3c03666
Nano Lett. 2024, 24, 1891−1900

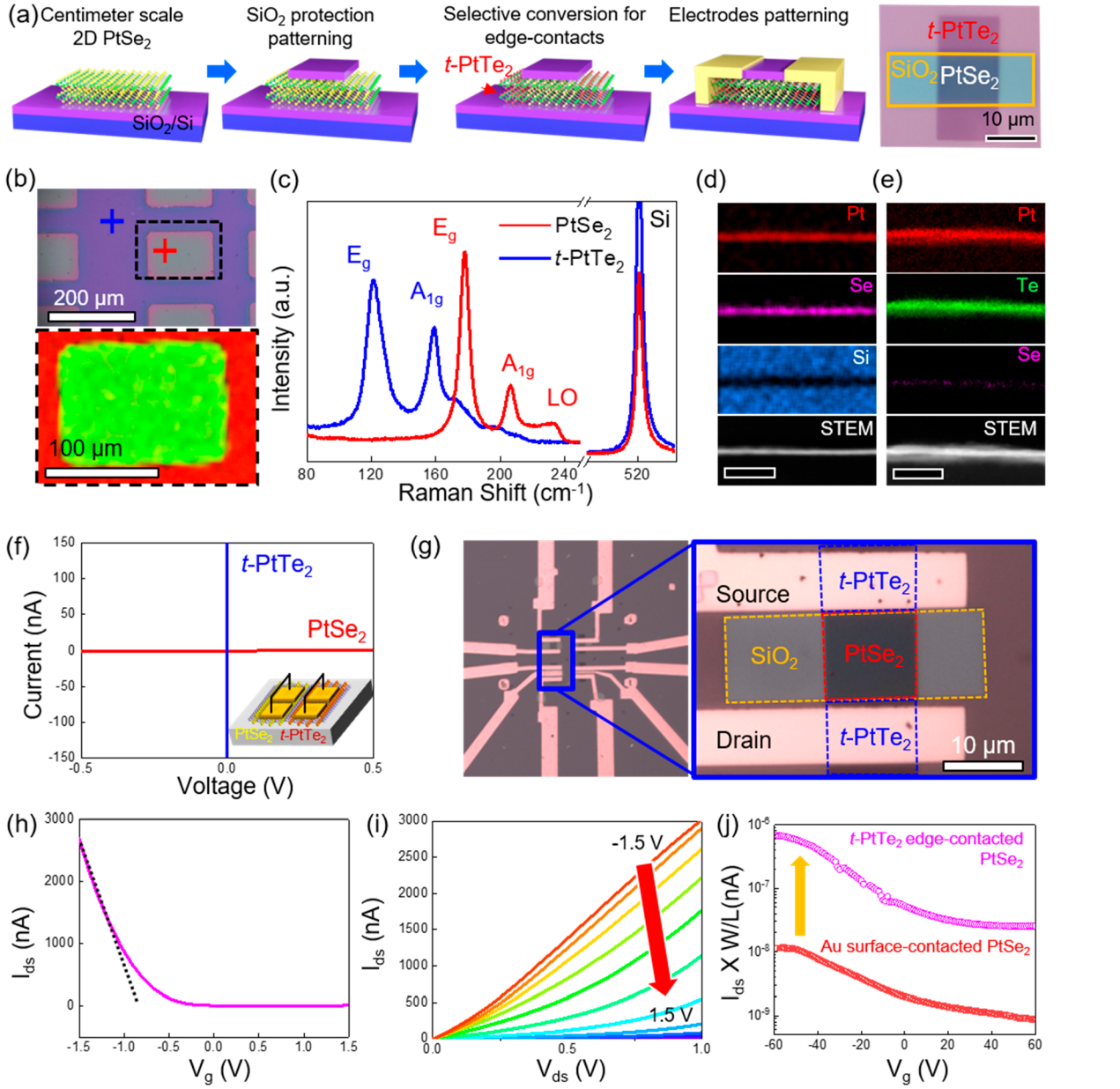

Figure 4. (a) Step-by-step procedure to fabricate patterns of 2D *t*-$PtTe_2$/$PtSe_2$/*t*-$PtTe_2$ in-plane heterolayers with edge contacts along with a representative OM image. (b) OM image of a fabricated array of the heterolayers with rectangular patterns (top) and Raman mapping image (bottom) corresponding to the black dotted box in the image (red region, 2D *t*-$PtTe_2$ layers; green region, 2D $PtSe_2$ layers). (c) Raman spectra obtained from the regions of 2D $PtSe_2$ layers (red cross mark in (b)) and 2D *t*-$PtTe_2$ layers (blue cross mark in (b)). (d, e) Cross-sectional EDS mapping images of (d) 2D $PtSe_2$ layers and (e) 2D *t*-$PtTe_2$ layers selected from the sample in (b). The scale bars in (d) and (e) are 20 nm. (f) *I*−*V* characteristics obtained from 2D *t*-$PtTe_2$ layers (blue) and 2D $PtSe_2$ layers (red) present within an identical sample along with their corresponding sample/measurement configuration (inset). (g) OM images of an array of FETs with 2D $PtSe_2$ channels edge-contacted with 2D *t*-$PtTe_2$ layers (zoomed-in view). (h, i) FET performances of an edge-contacted FET manifested by (h) I_{ds}−V_g characteristics at V_{ds} = 1 V and (i) I_{ds}−V_{ds} characteristics under varying gate voltages. (j) Comparison of normalized I_{ds}−V_g transfer curves for 2D-$PtSe_2$-layer-based FETs with 2D *t*-$PtTe_2$ layer edge contacts (purple) vs with Au surface contacts (red).

3d peak intensity significantly decreased after the transition (zoomed-in spectrum in Figure 2b, right inset). The atomic ratio of Pt:Te calculated from the XPS spectra is ∼32:68, indicating the stoichiometric transition of $PtSe_2$ to $PtTe_2$, which is a sharp contrast to the XPS observation before the transition. Next, we investigated the XPS characteristics of the materials undergoing the opposite transition direction of $PtTe_2$ to $PtSe_2$ (Figure 2c and d). We observed that the binding energy characteristics of Pt 4f, Te 3d (Figure 2c), and Se 3d (Figure 2d) exhibit exactly the opposite trend compared to the $PtSe_2$-to-$PtTe_2$ transition, confirming the high reversibility of this chemical transition. Furthermore, we performed Raman spectroscopy characterizations of the materials before and after their transition, and Figure 2e presents Raman spectra for the $PtSe_2$-to-$PtTe_2$ transition. Figure 2e (left) shows two vibration modes of in-plane (E_g) and out-of-plane (A_{1g}) at ∼178 and ∼206 cm^{-1}, respectively, obtained from pristine 2D $PtSe_2$ layers before their transition. The small hump at ∼235 cm^{-1} is attributed to a longitudinal optical (LO) mode corresponding to the superposition of A_{2u} and E_u modes.[22,32,36] Interestingly,

https://doi.org/10.1021/acs.nanolett.3c03666
Nano Lett. 2024, 24, 1891−1900

all of these $PtSe_2$ characteristic peaks disappeared after the transition and new peaks appeared at ∼120 and ∼159 cm^{-1}, which correspond to the E_g and A_{1g} modes of 2D $PtTe_2$ layers, respectively (Figure 2e, right). Raman characterizations were further performed to verify the reversibility of this transition. Figure 2f presents Raman characterizations of 2D $PtTe_2$ layers before/after their transition to 2D $PtSe_2$ layers, displaying an exactly opposite trend compared to Figure 2e. The originally observed $PtTe_2$ characteristic peaks (Figure 2f, left) disappeared after the transition, followed by an appearance of new peaks at different locations (Figure 2f, right). Also, the locations of all these E_g and A_{1g} peaks before/after the transition are consistent with previous studies,[23,25−27,32,37] confirming the transition reversibility. Lastly, energy-dispersive X-ray spectroscopy (EDS) characterizations were performed and corroborated with the XPS analysis. The EDS spectra obtained from the initial 2D $PtSe_2$ layers (Figure 2g) and 2D *t*-$PtTe_2$ layers (Figure 2h) reveal the stoichiometric ratios of Pt:Se = ∼33:66 and Pt:Te = ∼32:67 before/after the transition, respectively, which fully agrees with the XPS results.

Having verified the structural/chemical reversibility of the materials, we then explored their transition-driven electrical property modulations by characterizing FET gate responses. Figure 3a presents an output curve of drain-source current (I_{ds}) vs drain-source voltage (V_{ds}) from a 2D-$PtSe_2$-layer-based FET under varying back-gate voltage (V_g). The 2D $PtSe_2$ layers in their pristine form exhibit p-type semiconducting characteristics manifested by decreasing I_{ds} with increasing V_g from −60 to 60 V, consistent with recent studies.[22,23,25,38] Figure 3b compares two-terminal current−voltage (I−V) characteristics of 2D $PtSe_2$ layers before (red)/after (blue) their transition to 2D *t*-$PtTe_2$ layers, respectively. The inset presents a magnified I−V curve of 2D $PtSe_2$ layers before their transition was measured with Au contacts, showing excellent Ohmic transports irrespective of the transition. Interestingly, a significant conductivity increase (i.e., $>10^5$) is observed with this $PtSe_2$-to-$PtTe_2$ transition, i.e., ∼21.1 S/m for $PtSe_2$ (red) to ∼3.62 × 10^6 S/m for *t*-$PtTe_2$ (blue). Furthermore, the 2D *t*-$PtTe_2$ layers transited from 2D $PtSe_2$ layers exhibit strong metallic characteristics manifested by the complete overlap of I_{ds}−V_{ds} curves regardless of V_g, as shown in Figure 3c. This metallicity is consistent with previous studies on pristine 2D $PtTe_2$ layers,[26,27,37,39] which is a sharp contrast to the semiconducting characteristics observed before the transition. The reversibility of this semiconducting−metallic transition was also investigated for the materials undergoing the opposite transition of $PtTe_2$ to $PtSe_2$. Figure 3d presents that 2D $PtSe_2$ layers transited from initially metallic 2D $PtTe_2$ layers display p-type semiconducting characteristics similar to those of pristine 2D $PtSe_2$ layers (Figure 3a). I−V and FET transfer characteristics of the initial metallic 2D $PtTe_2$ layers before their transition are presented in the Supporting Information, Figure S2. Beyond these electrical verifications, we also performed optical characterizations to further clarify the semiconducting−metallic transition characteristics. Figure 3e presents ultraviolet−visible (UV−vis) spectroscopy absorbance spectra of materials before (red; $PtSe_2$) and after (blue; *t*-$PtTe_2$) the transition. The absorbance intensity of initial 2D $PtSe_2$ layers consistent with previous studies[40,41] is observed to slightly increase after their transition to 2D *t*-$PtTe_2$ layers. Figure 3f presents Tauc plots extracted from the absorbance spectra in Figure 3e in which α is the optical absorption coefficient and $h\nu$ is the photon energy.[39,42] The extrapolation of Tauc plots yields the optical bandgap of ∼0.5 eV for 2D $PtSe_2$ layers before the transition, confirming their semiconducting nature. Meanwhile 2D *t*-$PtTe_2$ layers do not exhibit a noticeable optical bandgap, which further supports the semiconducting-to-metallic transition verified in FET characterizations.

By leveraging these semiconducting−metallic transition characteristics, we explored a wafer-scale array of FETs containing in-plane heterolayers of 2D $PtSe_2$ seamlessly edge-contacted with 2D *t*-$PtTe_2$. Figure 4a illustrates the step-by-step FET fabrication procedure, which highlights the selective/patternable transition of 2D $PtSe_2$ layers to 2D *t*-$PtTe_2$ layers with the assistance of the SiO_2 protection layer. The semiconducting 2D $PtSe_2$ FET channels underneath the SiO_2 layer are edge-contacted with the metallic 2D *t*-$PtTe_2$ source/drain electrodes in an in-plane geometry, as demonstrated in the optical microscope (OM) image of an isolated pattern. Figure 4b presents a zoomed-in OM image (top) of the in-plane 2D heterolayers patterned on a large area ($>cm^2$) and a Raman mapping image (bottom) corresponding to the black dotted box. The color-mapped image confirms a highly localized distribution of 2D $PtSe_2$ layers (green) and 2D *t*-$PtTe_2$ layers (red). In Figure 4c, the red/blue Raman spectra obtained from the red/blue cross marks in Figure 4b, respectively, clearly evidence the patterned formation of 2D $PtSe_2$ layers and 2D *t*-$PtTe_2$ layers. Parts d and e of Figure 4 present cross-sectional EDS elemental mapping images of 2D $PtSe_2$ layers preserved underneath the SiO_2 layer and 2D *t*-$PtTe_2$ layers outside it, respectively. The images reveal the homogeneous localization of constituting Pt, Se, and Te in each targeted region, while their well-preserved stoichiometric compositions are verified in Figure S3 of the Supporting Information. The intermediate regime where Te and Se coexist at the $PtSe_2$/*t*-$PtTe_2$ interfaces was also confirmed by cross-sectional EDS analysis (Supporting Information, Figure S4.) Before investigating the exclusive influences of 2D *t*-$PtTe_2$ edge contacts on FET performances, we first examined the electrical conductance of 2D $PtSe_2$ and 2D *t*-$PtTe_2$ within the in-plane heterolayer corresponding to the Figure 4f inset. In Figure 4f, metallic 2D *t*-$PtTe_2$ layers exhibit a significantly higher conductance (i.e., $>10^5$, consistent with Figure 3b) over semiconducting 2D $PtSe_2$ layers. Figure 4g shows OM images of a representative FET displaying a laterally patterned array of *t*-$PtTe_2$/$PtSe_2$/*t*-$PtTe_2$ (zoomed-in view) fabricated by electron beam lithography (EBL) whose process details are presented in the Supporting Information, Experimental Section. Figure 4h presents transfer I_{ds}−V_g characteristics of a 2D *t*-$PtTe_2$ edge-contacted FET employing 2D $PtSe_2$ layers directly grown on a SiO_2/Si wafer, confirming its excellent p-type characteristics. The FET was operated under varying top-gate voltages, employing the protection SiO_2 layer as the gate dielectric. The FET hole mobility extracted from the linear slope[43] is ∼50.30 $cm^2\ V^{-1}\ s^{-1}$ which accompanies an on/off ratio of ∼248. These values are significantly higher than those of previously reported CVD-grown 2D $PtSe_2$ FETs[38,44,45] and are even comparable to the performances of mechanically exfoliated micrometer-sized 2D $PtSe_2$ FETs.[46,47] In fact, we comprehensively surveyed/compared the device performances of our edge-contacted 2D $PtSe_2$ FETs vs other 2D $PtSe_2$ FETs fabricated by various synthesis methods. The plot in Figure S5 of the Supporting Information confirms the high on/off ratio and carrier mobility values achieved in this study over previous reports.[21,38,44,45,48−51] Figure 4i presents the corresponding output curve of V_g-dependent I_{ds}−V_{ds}, further confirming the

https://doi.org/10.1021/acs.nanolett.3c03666
Nano Lett. 2024, 24, 1891−1900

prominent p-type characteristics. To clarify the exclusive role of the edge-contacts in FET performances, we prepared another batch of samples and studied their normalized $I_{ds}-V_{ds}$ characteristics under identical FET operation/geometry conditions. Figure 4j compares performances of 2D $PtSe_2$ FETs with 2D *t*-$PtTe_2$ layer edge-contacts (purple) vs with conventional Au surface-contacts without 2D *t*-$PtTe_2$ layers (red), obtained under identical back gating operations. The results show that the edge-contacted FET exhibits >50 times higher mobility and >2 times larger on/off ratios over the surface-contacted one. This remarkable enhancement is attributed to the significant reduction of the contact resistance in edge-contacted FETs. This was confirmed by the transmission line method (TLM) (Supporting Information, Experimental Section) identifying ∼5 times higher contact resistance of the surface-contacted FET (Supporting Information, Figure S6).

Lastly, we performed density functional theory (DFT) calculations to clarify the thermodynamic principle for the experimentally observed reversibility of the $PtSe_2-PtTe_2$ transition (Figure 5a) and its associated semiconducting–metallic modulation. Computational details are presented in the Supporting Information, Experimental Section. The reversible chemical transition is governed by the following reaction equation:

$$PtSe_2(solid) + 2Te(gas) \rightleftarrows PtTe_2(solid) + 2Se(gas)$$

The equation is based on the oxidation–reduction (redox.) reaction in the forward and reverse directions, respectively, as follows:

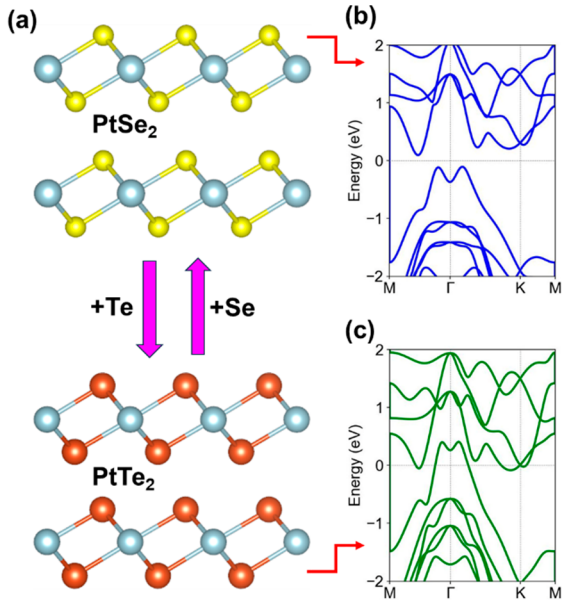

Figure 5. (a) Schematic illustration of the reversible reaction between semiconducting bilayer $PtSe_2$ and metallic bilayer $PtTe_2$. (b, c) Electronic dispersion in two-dimensional momentum space showing the transformation of bands under a reversible transition between (b) 2D $PtSe_2$ and (c) 2D $PtTe_2$ in bilayer forms. The crystal structure and symmetry group of both $PtSe_2$ and $PtTe_2$ are 1T-phase trigonal prismatic crystal structures and $P\bar{3}m1$ (No. 164). The lattice parameters are 3.8 and 4.0 Å for $PtSe_2$ and $PtTe_2$, respectively.

$$2Te^0 + 4e^- \rightarrow 2Te^{-II} \text{ (reduction)}$$

$$2Se^{-II} - 4e^- \rightarrow 2Se^0 \text{ (oxidation)}$$

and

$$2Se^0 + 4e^- \rightarrow 2Se^{-II} \text{ (reduction)}$$

$$2Te^{-II} - 4e^- \rightarrow 2Te^0 \text{ (oxidation)}$$

Here, Te and Se behave as oxidizing agents, whereas $PtSe_2$ and $PtTe_2$ act as reducing agents in the forward/reverse directions, respectively. We then investigated the reversible transformation in the electronic dispersion of semiconducting 2D $PtSe_2$ layers (Figure 5b) and metallic 2D $PtTe_2$ layers (Figure 5c) in a 2D momentum space. For simplicity, we considered the bilayers of both Pt-chalcogenides whose valence band (VB) and conduction band (CB) are plotted in blue and green colors, respectively. The bilayer $PtSe_2$ displays a band gap of 0.2 eV across the momentum space, whereas the bilayer $PtTe_2$ transformed from the $PtSe_2$ exhibits a metallic dispersion due to the size increase of chalcogen atoms (i.e., Se → Te) and stronger interlayer interactions. The red box in Figure 5c denotes the diffusion of VB into the CB driven by the chemical transition.

In conclusion, we studied the reversible transition of semiconducting 2D $PtSe_2$ layers and metallic 2D $PtTe_2$ layers and employed this approach in improving the FET performances. We emphasized several distinct advantages of this chemical transition process in creating 2D–2D semiconducting–metallic interfaces with excellent Ohmic transports, i.e., high scalabilty/patternability, low temperature reaction, and significantly reduced contact resistance. This unique superiority enabled the fabrication of a large-area patterned array of high-performance edge-contacted 2D FETs.

■ ASSOCIATED CONTENT

Supporting Information

The Supporting Information is available free of charge at https://pubs.acs.org/doi/10.1021/acs.nanolett.3c03666.

Experimental section, STEM images and grain boundary analysis, electrical characteristics of 2D $PtTe_2$ layers presenting metallic transports, EDS spectra obtained from 2D $PtSe_2$ layers and 2D *t*-$PtTe_2$ layers, cross-sectional EDS mapping images, plot of FET performance comparison, total resistance slopes as a function of FET channel lengths for edge- and surface-contacted FETs, and details of TLM for the contact resistance extraction (PDF)

■ AUTHOR INFORMATION

Corresponding Authors

Yeonwoong Jung − *NanoScience Technology Center and Department of Materials Science and Engineering, University of Central Florida, Orlando, Florida 32826, United States;* orcid.org/0000-0001-6042-5551; Email: yeonwoong.jung@ucf.edu

Hee-Suk Chung − *Electron Microscopy and Spectroscopy Team, Korea Basic Science Institute, Daejeon 34133, Republic of Korea*; Email: hschung13@kbsi.re.kr

Authors

Sang Sub Han − *NanoScience Technology Center, University of Central Florida, Orlando, Florida 32826, United States*

https://doi.org/10.1021/acs.nanolett.3c03666
Nano Lett. 2024, 24, 1891−1900

Shahid Sattar − *Department of Physics and Electrical Engineering, Linnaeus University, Kalmar SE-39231, Sweden;* orcid.org/0000-0003-4409-0100
Dmitry Kireev − *Department of Electrical and Computer Engineering and Microelectronics Research Center, The University of Texas at Austin, Austin, Texas 78758, United States; Department of Biomedical Engineering, University of Massachusetts Amherst, Amherst, Massachusetts 01003, United States;* orcid.org/0000-0003-1499-5435
June-Chul Shin − *NanoScience Technology Center, University of Central Florida, Orlando, Florida 32826, United States; Department of Materials Science and Engineering, Seoul National University, Seoul 08826, Republic of Korea*
Tae-Sung Bae − *Center for Research Equipment, Korea Basic Science Institute, Daejeon 34133, Republic of Korea*
Hyeon Ih Ryu − *Analytical Research Division, Korea Basic Science Institute, Jeonju 54907, Republic of Korea*
Justin Cao − *Department of Materials Science and Engineering, University of Central Florida, Orlando, Florida 32826, United States*
Alex Ka Shum − *Department of Mechanical and Aerospace Engineering, University of Central Florida, Orlando, Florida 32826, United States*
Jung Han Kim − *Department of Materials Science and Engineering, Dong-A University, Busan 49315, Republic of Korea;* orcid.org/0000-0002-6678-2282
Carlo Maria Canali − *Department of Physics and Electrical Engineering, Linnaeus University, Kalmar SE-39231, Sweden*
Deji Akinwande − *Department of Electrical and Computer Engineering and Microelectronics Research Center, The University of Texas at Austin, Austin, Texas 78758, United States;* orcid.org/0000-0001-7133-5586
Gwan-Hyoung Lee − *Department of Materials Science and Engineering, Seoul National University, Seoul 08826, Republic of Korea;* orcid.org/0000-0002-3028-867X

Complete contact information is available at: https://pubs.acs.org/10.1021/acs.nanolett.3c03666

Author Contributions

Y.J. conceived the project and directed it along with H.-S.C. S.S.H. prepared all of the samples and performed all device measurements and characteristic analysis with the assistance of A.K.S. and J.C. under the guidance of D.K., D.A., and Y.J. T.-S.B., H.I.R., and J.H.K. performed TEM characterizations under the guidance of H.-S.C. S.S. performed DFT calculations under the guidance of C.M.C. J.-C.S. participated in the fabrication and analysis of devices under the guidance of G.-H.L. D.K. participated in device performance evaluations under the guidance of D.A. S.S.H., D.K., D.A., and Y.J. wrote the manuscript with inputs from all authors.

Notes

The authors declare no competing financial interest.

■ ACKNOWLEDGMENTS

Y.J. acknowledges the support from the National Science Foundation (NSF) − CAREER award: 2142310. H.-S.C. was supported by the Electron Microscopy Team Program (C330221) funded by the Korea Basic Science Institute, Korea. T.-S.B. was supported by the Technology Innovation Program (20010542) funded by the MOTIE, Korea. J.H.K. acknowledges support from the Ministry of Science and ICT (Project Number: (2023) 2023-22030006-00) and the Commercialization Promotion Agency for R&D Outcomes (COMPA). D.A. acknowledges the National Science Foundation (NSF) Award Number DMR − 2308817 and the Cockrell Family Regents Chair Endowment. G.-H.L. acknowledges the support from the National Research Foundation (NRF) of Korea funded by the Ministry of Science, ICT & Future Planning (2021R1A2C3014316). S.S. and C.M.C. acknowledge support from the Swedish Research Council (VR) through Grant No. 2021-04622. The computations/data handling were enabled by resources provided by the National Academic Infrastructure for Supercomputing in Sweden (NAISS) at Dardel partially funded by the Swedish Research Council through Grant Agreement No. 2022-06725.

■ REFERENCES

(1) Gong, C.; Zhang, Y.; Chen, W.; Chu, J.; Lei, T.; Pu, J.; Dai, L.; Wu, C.; Cheng, Y.; Zhai, T.; et al. Electronic and Optoelectronic Applications Based on 2D Novel Anisotropic Transition Metal Dichalcogenides. *Adv. Sci.* **2017**, *4* (12), 1700231.
(2) Liu, C.; Chen, H.; Wang, S.; Liu, Q.; Jiang, Y. G.; Zhang, D. W.; Liu, M.; Zhou, P. Two-Dimensional Materials for Next-Generation Computing Technologies. *Nat. Nanotechnol* **2020**, *15* (7), 545−557.
(3) Allain, A.; Kang, J.; Banerjee, K.; Kis, A. Electrical Contacts to Two-Dimensional Semiconductors. *Nat. Mater.* **2015**, *14* (12), 1195−1205.
(4) Liu, Y.; Guo, J.; Zhu, E.; Liao, L.; Lee, S. J.; Ding, M.; Shakir, I.; Gambin, V.; Huang, Y.; Duan, X. Approaching the Schottky-Mott limit in van der Waals Metal-Semiconductor Junctions. *Nature* **2018**, *557* (7707), 696−700.
(5) Wang, Y.; Liu, S.; Li, Q.; Quhe, R.; Yang, C.; Guo, Y.; Zhang, X.; Pan, Y.; Li, J.; Zhang, H.; et al. Schottky Barrier Heights in Two-Dimensional Field-Effect Transistors: from Theory to Experiment. *Rep. Prog. Phys.* **2021**, *84* (5), 056501−056550.
(6) Chen, S.; Wang, S.; Wang, C.; Wang, Z.; Liu, Q. Latest Advance on Seamless Metal-Semiconductor Contact with Ultralow Schottky Barrier in 2D-Material-based Devices. *Nano Today* **2022**, *42*, 101372.
(7) Kim, C.; Moon, I.; Lee, D.; Choi, M. S.; Ahmed, F.; Nam, S.; Cho, Y.; Shin, H. J.; Park, S.; Yoo, W. J. Fermi Level Pinning at Electrical Metal Contacts of Monolayer Molybdenum Dichalcogenides. *ACS Nano* **2017**, *11* (2), 1588−1596.
(8) Yoon, Y.; Ganapathi, K.; Salahuddin, S. How Good Can Monolayer MoS_2 Transistors be? *Nano Lett.* **2011**, *11* (9), 3768−3773.
(9) Gong, C.; Colombo, L.; Wallace, R. M.; Cho, K. The Unusual Mechanism of Partial Fermi Level Pinning at Metal-MoS_2 Interfaces. *Nano Lett.* **2014**, *14* (4), 1714−1720.
(10) Chen, R.-S.; Ding, G.; Zhou, Y.; Han, S.-T. Fermi-Level Depinning of 2D Transition Metal Dichalcogenide Transistors. *J. Mater. Chem. C Mater.* **2021**, *9* (35), 11407−11427.
(11) Khalil, H. M.; Khan, M. F.; Eom, J.; Noh, H. Highly Stable and Tunable Chemical Doping of Multilayer WS_2 Field Effect Transistor: Reduction in Contact Resistance. *ACS Appl. Mater. Interfaces* **2015**, *7* (42), 23589−23596.
(12) Song, S.; Yoon, A.; Ha, J. K.; Yang, J.; Jang, S.; Leblanc, C.; Wang, J.; Sim, Y.; Jariwala, D.; Min, S. K.; et al. Atomic Transistors Based on Seamless Lateral Metal-Semiconductor Junctions with a Sub-1-nm Transfer Length. *Nat. Commun.* **2022**, *13* (1), 4916.
(13) Zhao, Y.; Xu, K.; Pan, F.; Zhou, C.; Zhou, F.; Chai, Y. Doping, Contact and Interface Engineering of Two-Dimensional Layered Transition Metal Dichalcogenides Transistors. *Adv. Funct. Mater.* **2017**, *27* (19), 1603484.
(14) Gong, Y.; Yuan, H.; Wu, C. L.; Tang, P.; Yang, S. Z.; Yang, A.; Li, G.; Liu, B.; van de Groep, J.; Brongersma, M. L.; et al. Spatially Controlled Doping of Two-Dimensional SnS_2 Through Intercalation for Electronics. *Nat. Nanotechnol* **2018**, *13* (4), 294−299.
(15) Du, Y.; Liu, H.; Neal, A. T.; Si, M.; Ye, P. D. Molecular Doping of Multilayer MoS_2 Field-Effect Transistors: Reduction in Sheet and

Contact Resistances. *IEEE Electron Device Lett.* **2013**, *34* (10), 1328−1330.
(16) Kim, Y.-H.; Kang, M.-S.; Choi, J. W.; Lee, W.-Y.; Kim, M.-J.; Park, N.-W.; Yoon, Y.-G.; Kim, G.-S.; Lee, S.-K. Barrier-Free Semimetallic $PtSe_2$ Contact Formation in Two-Dimensional $PtSe_2$/$PtSe_2$ Homostructure for High-Performance Field-Effect Transistors. *Appl. Surf. Sci.* **2023**, *638*, 158061.
(17) Su, S.-H.; Hsu, W.-T.; Hsu, C.-L.; Chen, C.-H.; Chiu, M.-H.; Lin, Y.-C.; Chang, W.-H.; Suenaga, K.; He, J.-H.; Li, L.-J. Controllable Synthesis of Band-Gap-Tunable and Monolayer Transition-Metal Dichalcogenide Alloys. *Front. Energy Res.* **2014**, *2*, 1−8.
(18) Mahjouri-Samani, M.; Lin, M.-W.; Wang, K.; Lupini, A. R.; Lee, J.; Basile, L.; Boulesbaa, A.; Rouleau, C. M.; Puretzky, A. A.; Ivanov, I. N.; et al. Patterned Aarrays of Lateral Heterojunctions within Monolayer Two-dimensional Semiconductors. *Nat. Commun.* **2015**, *6*, 7749−7754.
(19) Taghinejad, H.; Rehn, D. A.; Muccianti, C.; Eftekhar, A. A.; Tian, M.; Fan, T.; Zhang, X.; Meng, Y.; Chen, Y.; Nguyen, T. V.; et al. Defect-Mediated Alloying of Monolayer Transition-Metal Dichalcogenides. *ACS Nano* **2018**, *12* (12), 12795−12804.
(20) Yun, S. J.; Han, G. H.; Kim, H.; Duong, D. L.; Shin, B. G.; Zhao, J.; Vu, Q. A.; Lee, J.; Lee, S. M.; Lee, Y. H. Telluriding Monolayer MoS_2 and WS_2 via Alkali Metal Scooter. *Nat. Commun.* **2017**, *8* (1), 2163.
(21) Kim, H.-S.; Jeong, J.; Kwon, G.-H.; Kwon, H.; Baik, M.; Cho, M.-H. Improvement of Electrical Performance Using $PtSe_2$/$PtTe_2$ Edge Contact Synthesized by Molecular Beam Epitaxy. *Appl. Surf. Sci.* **2022**, *585*, 152507.
(22) Han, S. S.; Kim, J. H.; Noh, C.; Kim, J. H.; Ji, E.; Kwon, J.; Yu, S. M.; Ko, T. J.; Okogbue, E.; Oh, K. H.; et al. Horizontal-to-Vertical Transition of 2D Layer Orientation in Low-Temperature Chemical Vapor Deposition-Grown $PtSe_2$ and Its Influences on Electrical Properties and Device Applications. *ACS Appl. Mater. Interfaces* **2019**, *11* (14), 13598−13607.
(23) Okogbue, E.; Han, S. S.; Ko, T. J.; Chung, H. S.; Ma, J.; Shawkat, M. S.; Kim, J. H.; Kim, J. H.; Ji, E.; Oh, K. H.; et al. Multifunctional Two-Dimensional $PtSe_2$-Layer Kirigami Conductors with 2000% Stretchability and Metallic-to-Semiconducting Tunability. *Nano Lett.* **2019**, *19* (11), 7598−7607.
(24) Okogbue, E.; Ko, T. J.; Han, S. S.; Shawkat, M. S.; Wang, M.; Chung, H. S.; Oh, K. H.; Jung, Y. Wafer-scale 2D $PtTe_2$ layers for high-efficiency mechanically flexible electro-thermal smart window applications. *Nanoscale* **2020**, *12* (19), 10647−10655.
(25) Shawkat, M. S.; Gil, J.; Han, S. S.; Ko, T. J.; Wang, M.; Dev, D.; Kwon, J.; Lee, G. H.; Oh, K. H.; Chung, H. S.; et al. Thickness-Independent Semiconducting-to-Metallic Conversion in Wafer-Scale Two-Dimensional $PtSe_2$ Layers by Plasma-Driven Chalcogen Defect Engineering. *ACS Appl. Mater. Interfaces* **2020**, *12* (12), 14341−14351.
(26) Wang, M.; Ko, T. J.; Shawkat, M. S.; Han, S. S.; Okogbue, E.; Chung, H. S.; Bae, T. S.; Sattar, S.; Gil, J.; Noh, C.; et al. Wafer-Scale Growth of 2D $PtTe_2$ with Layer Orientation Tunable High Electrical Conductivity and Superior Hydrophobicity. *ACS Appl. Mater. Interfaces* **2020**, *12* (9), 10839−10851.
(27) Ko, T.-J.; Han, S. S.; Okogbue, E.; Shawkat, M. S.; Wang, M.; Ma, J.; Bae, T.-S.; Hafiz, S. B.; Ko, D.-K.; Chung, H.-S.; et al. Wafer-scale 2D $PtTe_2$ layers-enabled Kirigami heaters with superior mechanical stretchability and electro-thermal responsiveness. *Appl. Mater. Today* **2020**, *20*, 100718−100727.
(28) Zeng, L. H.; Lin, S. H.; Li, Z. J.; Zhang, Z. X.; Zhang, T. F.; Xie, C.; Mak, C. H.; Chai, Y.; Lau, S. P.; Luo, L. B.; Tsang, Y. H. Photodetectors: Fast, Self-Driven, Air-Stable, and Broadband Photodetector Based on Vertically Aligned $PtSe_2$/GaAs Heterojunction. *Adv. Funct Mater.* **2018**, *28* (16), 1705970−1705980.
(29) Ma, H.; Qian, Q.; Qin, B.; Wan, Z.; Wu, R.; Zhao, B.; Zhang, H.; Zhang, Z.; Li, J.; Zhang, Z.; et al. Controlled Synthesis of Ultrathin $PtSe_2$ Nanosheets with Thickness-Tunable Electrical and Magnetoelectrical Properties. *Adv. Sci.* **2022**, *9* (1), No. e2103507.
(30) Li, J.; Kolekar, S.; Ghorbani-Asl, M.; Lehnert, T.; Biskupek, J.; Kaiser, U.; Krasheninnikov, A. V.; Batzill, M. Layer-Dependent Band Gaps of Platinum Dichalcogenides. *ACS Nano* **2021**, *15* (8), 13249−13259.
(31) Hao, S.; Zeng, J.; Xu, T.; Cong, X.; Wang, C.; Wu, C.; Wang, Y.; Liu, X.; Cao, T.; Su, G.; et al. Low-Temperature Eutectic Synthesis of $PtTe_2$ with Weak Antilocalization and Controlled Layer Thinning. *Adv. Funct. Mater.* **2018**, *28* (36), 1803746.
(32) Gong, Y.; Lin, Z.; Chen, Y. X.; Khan, Q.; Wang, C.; Zhang, B.; Nie, G.; Xie, N.; Li, D. Two-Dimensional Platinum Diselenide: Synthesis, Emerging Applications, and Future Challenges. *Nanomicro Lett.* **2020**, *12* (1), 174.
(33) Villaos, R. A. B.; Crisostomo, C. P.; Huang, Z.-Q.; Huang, S.-M.; Padama, A. A. B.; Albao, M. A.; Lin, H.; Chuang, F.-C. Thickness Dependent Electronic Properties of Pt Dichalcogenides. *NPJ. 2D Mater. Appl.* **2019**, *3* (1), 2.
(34) Furuseth, S.; Selte, K.; Kjekshus, A.; Gronowitz, S.; Hoffman, R. A.; Westerdahl, A. Redetermined Crystal Structures of $NiTe_2$, $PdTe_2$, PtS_2, $PtSe_2$, and $PtTe_2$. *Acta Chem. Scand.* **1965**, *19*, 257−258.
(35) Zhussupbekov, K.; Ansari, L.; McManus, J. B.; Zhussupbekova, A.; Shvets, I. V.; Duesberg, G. S.; Hurley, P. K.; Gity, F.; Ó Coileáin, C.; McEvoy, N. Imaging and Identification of Point Defects in $PtTe_2$. *NPJ. 2D Mater. Appl.* **2021**, *5* (1), 1−10.
(36) Yan, M.; Wang, E.; Zhou, X.; Zhang, G.; Zhang, H.; Zhang, K.; Yao, W.; Lu, N.; Yang, S.; Wu, S.; et al. High Quality Atomically Thin $PtSe_2$ Films Grown by Molecular Beam Epitaxy. *2D Materials* **2017**, *4* (4), 045015.
(37) Han, S. S.; Shawkat, M. S.; Lee, Y. H.; Park, G.; Li, H.; Chung, H.-S.; Yoo, C.; Mofid, S. A.; Sattar, S.; Choudhary, N.; et al. Wafer-Scale Anion Exchange Conversion of Nonlayered PtS Films to van der Waals Two-Dimensional $PtTe_2$ Layers with Negative Photoresponsiveness. *Chem. Mater.* **2022**, *34* (15), 6996−7005.
(38) Ansari, L.; Monaghan, S.; McEvoy, N.; Coileáin, C. Ó.; Cullen, C. P.; Lin, J.; Siris, R.; Stimpel-Lindner, T.; Burke, K. F.; Mirabelli, G.; et al. Quantum Confinement-Induced Semimetal-to-Semiconductor Evolution in Large-Area Ultra-Thin $PtSe_2$ Films Grown at 400 °C. *NPJ. 2D Mater. Appl.* **2019**, *3* (1), 33.
(39) Han, S. S.; Ko, T. J.; Shawkat, M. S.; Shum, A. K.; Bae, T. S.; Chung, H. S.; Ma, J.; Sattar, S.; Hafiz, S. B.; Mahfuz, M. M. A.; et al. Peel-and-Stick Integration of Atomically Thin Nonlayered PtS Semiconductors for Multidimensionally Stretchable Electronic Devices. *ACS Appl. Mater. Interfaces* **2022**, *14* (17), 20268−20279.
(40) Li, Z.; Li, R.; Pang, C.; Dong, N.; Wang, J.; Yu, H.; Chen, F. 8.8 GHz Q-switched Mode-Locked Waveguide Lasers Modulated by $PtSe_2$ Saturable Absorber. *Opt Express* **2019**, *27* (6), 8727−8737.
(41) Yuan, J.; Mu, H.; Li, L.; Chen, Y.; Yu, W.; Zhang, K.; Sun, B.; Lin, S.; Li, S.; Bao, Q. Few-Layer Platinum Diselenide as a New Saturable Absorber for Ultrafast Fiber Lasers. *ACS Appl. Mater. Interfaces* **2018**, *10* (25), 21534−21540.
(42) TAUC, J.; GRIGOROVIC, R.; VANCU, A. Optical Properties and Electronic Structure of Ge. *Phys. Status Solidi* **1966**, *15*, 627−637.
(43) Streetman, B. G.; Banerjee, S. *Solid State Electronic Devices*; Prentice Hall: 2000.
(44) Jiang, W.; Wang, X.; Chen, Y.; Wu, G.; Ba, K.; Xuan, N.; Sun, Y.; Gong, P.; Bao, J.; Shen, H.; et al. Large-area High Quality $PtSe_2$ Thin Film with Versatile Polarity. *InfoMat* **2019**, *1* (2), 260−267.
(45) Wang, Z.; Li, Q.; Besenbacher, F.; Dong, M. Facile Synthesis of Single Crystal $PtSe_2$ Nanosheets for Nanoscale Electronics. *Adv. Mater.* **2016**, *28* (46), 10224−10229.
(46) Zhao, Y.; Qiao, J.; Yu, Z.; Yu, P.; Xu, K.; Lau, S. P.; Zhou, W.; Liu, Z.; Wang, X.; Ji, W.; Chai, Y. High-Electron-Mobility and Air-Stable 2D Layered $PtSe_2$ FETs. *Adv. Mater.* **2017**, *29* (5), 1604230.
(47) Ciarrocchi, A.; Avsar, A.; Ovchinnikov, D.; Kis, A. Thickness-Modulated Metal-to-Semiconductor Transformation in a Transition Metal Dichalcogenide. *Nat. Commun.* **2018**, *9* (1), 919.
(48) Kim, H.-S.; Jeong, J.; Kwon, G.-H.; Park, S.; Jeong, K.; Choi, Y.-H.; Kwon, H.; Baik, M.; Im, S.; Cho, M.-H. Ultrathin Platinum Diselenide Synthesis Controlling Initial Growth Kinetics: Interfacial

https://doi.org/10.1021/acs.nanolett.3c03666
Nano Lett. 2024, 24, 1891−1900

Reaction Depending on Thickness and Substrate. *Appl. Surf. Sci.* **2021**, *564*, 150300.
(49) Xu, H.; Zhang, H.; Liu, Y.; Zhang, S.; Sun, Y.; Guo, Z.; Sheng, Y.; Wang, X.; Luo, C.; Wu, X.; et al. Controlled Doping of Wafer-Scale $PtSe_2$ Films for Device Application. *Adv. Funct. Mater.* **2019**, *29* (4), 1805614.
(50) Li, L.; Xiong, K.; Marstell, R. J.; Madjar, A.; Strandwitz, N. C.; Hwang, J. C. M.; McEvoy, N.; McManus, J. B.; Duesberg, G. S.; Goritz, A.; et al. Wafer-Scale Fabrication of Recessed-Channel $PtSe_2$ MOSFETs With Low Contact Resistance and Improved Gate Control. *IEEE Trans. Electron Devices* **2018**, *65* (10), 4102−4108.
(51) Xiong, K.; Hilse, M.; Li, L.; Goritz, A.; Lisker, M.; Wietstruck, M.; Kaynak, M.; Engel-Herbert, R.; Madjar, A.; Hwang, J. C. M. Large-Scale Fabrication of Submicrometer-Gate-Length MOSFETs With a Trilayer $PtSe_2$ Channel Grown by Molecular Beam Epitaxy. *IEEE Trans. Electron Devices* **2020**, *67* (3), 796−801.

https://doi.org/10.1021/acs.nanolett.3c03666
Nano Lett. 2024, 24, 1891−1900